Pergamon

Int. J. Heat Mass Transfer. Vol. 40, No. 10, pp. 2283–2292, 1997

0017–9310/97 $17.00+0.00

PII: S0017–9310(96)00314–6

Three-dimensional analytical temperature field and its application to solidification characteristics in high- or low-power-density-beam welding

P. S. WEI, C. Y. HO, M. D. SHIAN and C. L. HU

Institute of Mechanical Engineering, National Sun Yat-Sen University, Kaohsiung, Taiwan, China

(*Received* 8 *February* 1996 *and in final form* 27 *August* 1996)

Abstract—An analytical three-dimensional temperature field in the liquid and heat-affected zones around the welding cavity produced by a moving high-intensity beam is provided. The cavity is idealized by a paraboloid of revolution in a semi-infinite workpiece subject to an incident flux of a Gaussian distribution. A relevant image technique is introduced to account for the adiabatic top surface. Three-dimensional solidification characteristics of the fusion zone, therefore, are quantitatively determined. The results show the effects of welding parameters, such as the dimensionless beam power, Peclet number, cavity opening radius, preheating temperature, and the parameter approximating convection, on the shape of the fusion zone, the cooling rates, and morphological stability. The findings agree well with available experimental data and three-dimensional finite-difference results.

INTRODUCTION

A temperature field is required to predict not only welding processes but also microstructures of workpieces. Microstructures including the size and shape of grains, segregation, hot cracking and porosity of the fusion zone are primarily determined by the solidification speed and liquid temperature gradient at the solidification front [1, 2]. Unfortunately, a general and quantitative understanding of three-dimensional solidification characteristics in higher-power-density-beam welding is still lacking. Providing an analytical solution of three-dimensional temperature and applying it to solidification characteristics in high- or low-power-density-beam welding become the objectives of this work.

One of the first investigations into the growth of substructures in tungsten arc or low-power-density-beam welds was by Calvo *et al.* [3]. They found that an increase in the alloy content of the pool, or a decrease in the thermal gradient, caused the microstructure to change from the planar to cellular-dendritic forms and ultimately free dendritic modes. Being similar to the solidification of castings the mechanism of constitutional supercooling, first proposed by Rutter and Chalmers [4], was used for producing an interpretation. That is, the higher the degree of constitutional supercooling or the smaller G_l/V_n, the greater the tendency for a given material to switch from planar, cellular to a dendritic microstructure.

The relevancy of constitutional supercooling in welding was also confirmed from experimental observations [5, 6]. In a horizontal cross-section the growth of the fusion boundary is the lowest while the normal temperature gradient is the steepest. As the weld centerline is approached along the solidification front, the growth rate increases and normal temperature gradient decreases. Microstructures, therefore, were observed to vary from the planar, columnar, columnar dendrite and equiaxed dendrite from the fusion boundary to weld centerline [7].

Microstructures are also related to the sizes and spacings of the primary and secondary dendrite arms of the solidification front. Brown and Adams [8] measured dendrite spacings of 2014 aluminum alloys in arc welds and found that the dendrite arm spacing would be proportional to the square root of the power-to-welding speed ratio. A simplified one-dimensional conservation equation of solute was derived and a successful comparison was made by Brown and Adams [9]. Subsequent works by Jordan and Coleman [10] for welding an Al–Mg–Mn alloy and Lanzafame and Kattamis [11] for welding 2014 aluminum alloy, have substantiated this relationship. The latter also found that the dendrite arm spacings vary from the fusion boundary to weld centerline, being finer at the centerline. This is primarily due to the variation in local solidification time.

Katayama and Matsunawa [12] measured the primary arm spacings of a stainless steel for different welding speeds and depths of the fusion zone in high-power-density-beam welding. The primary arm spacings and cooling rates (G_lV_n) were correlated. The measured primary arm spacings were around 10^{-6} m. The average primary arm spacing increased significantly as the welding speed became less than 0.03 m s^{-1}.

NOMENCLATURE

C_0 initial solid concentration
D liquid solutal diffusivity
G_l liquid temperature gradient at solidification front
h dimensionless cavity depth $= \hat{h}/\hat{\sigma}$
H $h_{lg}/R(T_m - T_\infty)$
h' dimensionless length, as illustrated in Fig. 1
h_{lg} latent heat of evaporation
k thermal conductivity
k_e equilibrium partition coefficient
L_{p-1}^m Laguerre function
m slope of liquidus line in phase diagram
p_b boiling pressure
P $p_b\hat{\sigma}/\gamma_m$
Pe Peclet number $= U\hat{\sigma}/\alpha$
Q beam power
Q^* dimensionless beam power $= Q/k_l\hat{\sigma}(T_m - T_\infty)$
r radial coordinate $= \hat{r}/\hat{\sigma}$
R gas constant
r_0 dimensionless cavity opening radius $= \hat{r}_0/\hat{\sigma}$
S parameter approximating convection $= \alpha/\alpha_z$
t dimensional time
T, T_∞ dimensional temperature and ambient temperature
U dimensional welding speed
V_n local solidification speed
Y $(T_m - T_\infty)(d\gamma/dT)/\gamma_m$ where $d\gamma/dT$ is a constant
x, y, z Cartesian coordinates as shown in Fig. 1, $x = \hat{x}/\hat{\sigma}$, $y = \hat{y}/\hat{\sigma}$, $z = \hat{z}/\hat{\sigma}$.

Greek letters
α, α_z liquid diffusivity, enhanced diffusivity in vertical direction
γ surface tension
Γ gamma function
η, η_0 parabolic coordinate and coordinate on cavity surface, as shown in Fig. 1
θ dimensionless temperature $= (T - T_\infty)/(T_m - T_\infty)$
θ_b, θ_B boiling point and cavity base temperature
θ_∞ $T_\infty/(T_m - T_\infty)$
Λ liquid to solid thermal diffusivity ratio
ξ, ξ_e parabolic coordinate and coordinate at cavity opening, $\xi_e = hPe\sqrt{S}$, as shown in Fig. 1
$\hat{\sigma}$ beam energy distribution parameter
ϕ parabolic coordinate, as shown in Fig. 1
Ψ confluent hypergeometric function of the second kind.

Superscript
$\hat{}$ dimensional quantity
$'$ imaged coordinate.

Subscript
m melting.

Kou *et al.* [13] numerically computed a three-dimensional energy equation in a workpiece subject to a laser-beam of Gaussian and uniform flux distributions. Assuming no cavity was formed and allowing for the evolution of latent heat both the maximum cooling rate and the most unstable solidification front were found to occur near the weld centerline at the top surface.

The most widely used models to predict temperature fields in low- or high-power-density-beam welding have been the point- and line-source solutions, as first used by Rosenthal [14]. However, these simplified models in their pristine forms exhibit defects such as the occurrence of infinite temperatures near sources, ignorances of the distribution of incident flux, convective effect, vertical heat transfer for the line source, and the balance of momentum. Hence, the prediction of microstructure has been neither possible nor reliable on that basis. To eliminate the above defects, Wei and Shian [15] provided a new three-dimensional analytical solution for the temperature field around the cavity of a paraboloid of revolution produced by a high-power-density beam. However, in view of the cavity the introduced image method cannot simulate accurately the effects of the adiabatic surfaces, as can be seen later.

In this study, an analytical temperature field by satisfying exactly the adiabatic condition at the top surface via introducing a new image method is provided. A simple and relevant prediction of microstructures in the fusion zone therefore is achieved.

SYSTEM MODEL AND ANALYSIS

A workpiece is moved with a constant speed relative to the energy-beam, as illustrated in Fig. 1. Since the beam energy continuously irradiates on the top surface a deep and narrow vapor-filled cavity surrounded by liquid and solid regions can be produced. Welding occurs as the liquid flow from the front to the rear [16–19]. In this work, aside from a quasi-steady-state, surface heat source, averaged thermal and physical

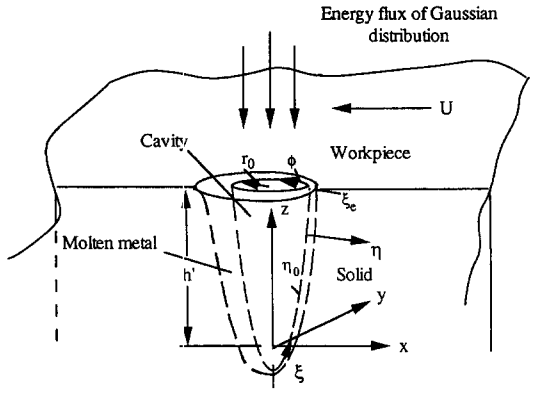

Fig. 1. Physical model and coordinate system.

properties, and identical thermal conductivity of solid and liquid [15], other assumptions made need to be described as follows:

(1) The incident flux is a Gaussian distribution at any transverse cross-section. Hicken *et al.* [20] confirmed this fact by measuring incident flux at vertical distances within about 0.635 cm that deviated from the focal spot of an electron-beam. A laser-beam of a Gaussian distribution is valid for the spatially coherent TEM_{00} model [21]. Energy fluxes absorbed can also be represented as Gaussian distributions for the radiative absorptivity of unity, or a cavity depth-to-opening radius ratio greater than 5 [22], or else the focal spot lower than the cavity base [23].

(2) The cavity is idealized by a paraboloid of revolution to a first approximation. The cavity can be a cone, paraboloid of revolution, or other irregular geometries during welding. For welding with a moving heat source, the geometry also becomes slightly asymmetric [24]. The cavity, however, was roughly observed to be a paraboloid of revolution near the cavity base [25]. Consistent theoretical results can be seen in Refs. [24, 26–28].

(3) Absorption within the plasma in the cavity is ignored. Temperatures and concentrations of electrons in iron plasmas during deep welding with a continuous CO_2 laser were measured by Poueyo-Verwaerde *et al.* [29] and Collur and DebRoy [30] to be as high as 7000 K and 9×10^{23} particles/m^3, respectively. The absorption length due to electron–neutral interactions therefore is 0.25 m while that resulting from electron-ionized iron is 0.03 m. As a consequence, $80\%\pm10\%$ of a beam power of 15 kW and $92\%\pm5\%$ of 1 kW are transmitted. Inverse Brehmstrahlung absorption [31] was similarly found to be 1 m for aluminum and titanium plasmas irradiated by a continuous CO_2 laser [32] and pulsed YAG laser [33], respectively. Radiation from the plasma and Rayleigh and Mie scatterings of the beam can also be ignored [33]. Even though radiative transport has been approximately and complicatedly modeled [28, 34, 35], the plasma generally can be considered as a transparent medium under working conditions such as an electron-beam as the heat source [36], an energy-beam with a small wavelength (e.g. Nd: YAG laser), low pressure of the surroundings, and vapor having a low ionization threshold.

(4) Latent heats due to evaporation and melting or solidification are neglected [37]. For example, in welding aluminum with a beam power of 3 kW evaporation rate is around 10^{-5} kg s^{-1} [30, 38], which leads to the latent heat due to evaporation of 100 W. The maximum latent heat for solidification occurring near the top surface is less than 5% of heat conduction ($\sim10^8$ Wm^{-2}) as estimated from a pool thickness of 10^{-3} m, temperature difference of 10^3 K and welding speed of 5×10^{-3} ms^{-1}.

(5) Vapor pressure and surface tension are balanced at the cavity base. In reality, liquid pressure should be accounted for. However, it is at most of the same magnitude as the vapor pressure, which can be 4000 Pa corresponding to a saturation temperature of 2100 K [25, 27]. Since vapor pressure is strongly dependent on temperature, the difference in temperature is no more than 100 K without including liquid pressure.

(6) Thermal diffusivity is nonisotropic in order to account for convection. Since the flow of liquid enhances energy transport, the diffusivity in the flow direction is increased by a constant multiple of around 5 [39, 40]. This assumption is a rough approximation. A further study of the enhanced diffusivity is required.

Analytical temperature induced by a ring-source

With the above assumptions, the heat conduction equation becomes

$$-U\frac{\partial T}{\partial \hat{x}}=\alpha\left(\frac{\partial^2 T}{\partial \hat{x}^2}+\frac{\partial^2 T}{\partial \hat{y}^2}\right)+\alpha_z\frac{\partial^2 T}{\partial \hat{z}^2}. \tag{1}$$

Introducing

$$v=[(T-T_\infty)/(T_m-T_\infty)]\exp(\sqrt{\xi\eta}\cos\phi)$$

eqn (1) becomes

$$\frac{4}{\xi+\eta}\left[\frac{\partial}{\partial\xi}\left(\xi\frac{\partial v}{\partial\xi}\right)+\frac{\partial}{\partial\eta}\left(\eta\frac{\partial v}{\partial\eta}\right)+\frac{1}{4}\left(\frac{1}{\xi}+\frac{1}{\eta}\right)\frac{\partial^2 v}{\partial\phi^2}\right]=v \tag{2}$$

where the parabolic coordinates are related to the Cartesian coordinate systems by

$$\xi=\frac{Pe}{2}(z\sqrt{S}+\sqrt{x^2+y^2+Sz^2}),$$

$$\eta=\frac{Pe}{2}(-z\sqrt{S}+\sqrt{x^2+y^2+Sz^2}),$$

$$\phi=\tan^{-1}\left(\frac{y}{x}\right). \tag{3}$$

The solution of eqn (2) can be found from the separation-of-variables method

$$v\sim[\xi^{m/2}\,e^{-\xi/2}L_{p-1}^{m}(\xi)]\times[\eta^{m/2}\,e^{-\eta/2}\Psi(m+p,m+1,\eta)]\cos(m\phi) \tag{4}$$

where the functions L^m_{p-1} and Ψ are the Laguerre function and confluent hypergeometric function of the second kind, respectively. The former and the latter become infinity as the arguments approach infinity and zero, respectively. Therefore, a general solution of eqn (1) subject to finite temperatures far from the cavity is [15]

$$\theta = \frac{3Q^*\sqrt{S}}{\pi Pe}\exp\left(-\sqrt{\xi\eta}\cos\phi - \frac{\eta+\xi}{2}\right)$$

$$\sum_{m=0}^{\infty}\sum_{p=1}^{\infty}\tilde{A}_{m,p}(\xi\eta)^{m/2}L^m_{p-1}(\xi)\Psi(m+p,m+1,\eta)\cos(m\phi)$$

$$\eta \geqslant \eta_0. \quad (5)$$

In this work, dividing incident flux into ring-elements is proposed in order to apply an image technique. An energy balance between conduction and a ring element of incident flux at $\xi = \xi_i$ on the cavity wall can be described by

$$\frac{\partial v}{\partial \eta} = -\frac{3Q^*\sqrt{S}}{\pi Pe}\exp\left(\sqrt{\xi\eta_0}\cos\phi - \frac{12\xi\eta_0}{Pe^2}\right)\delta(\xi-\xi_i) \quad (6)$$

where the delta function $\delta(\xi-\xi_i) = 0$ if $\xi \neq \xi_i$. Substituting eqn (5) into eqn (6), multiplying the resulting equation by $\cos(m\phi)$, $\xi^{m/2}$, $\exp(-\xi/2)$, and $L^m_{p-1}(\xi)$, integrating over ϕ and ξ [41], and using the orthogonal properties of cosine and Laguerre functions the coefficients give

$$\tilde{A}_{m,p} = \left(\frac{1}{2}\right)^{\delta_{m0}}\frac{2\Gamma(p)}{\Gamma(m+p)}\left(\frac{\xi_i}{\eta_0}\right)^{m/2} I_m(\sqrt{\xi_i\eta_0})L^m_{p-1}(\xi_i)$$

$$\times \exp\left(-\frac{12\xi_i\eta_0}{Pe^2} - \frac{\xi_i-\eta_0}{2}\right)\Bigg/$$

$$\left[\left(\frac{1}{2}-\frac{m}{2\eta_0}\right)\Psi(m+p,m+1,\eta_0)\right.$$

$$\left.+(m+p)\Psi(m+p+1,m+2,\eta_0)\right] \quad (7)$$

where the modified Bessel function of the first kind appears for a ring source. Temperatures predicted by using $m = 0$ are sufficiently accurate with errors of less than 3%.

Temperature in a semi-infinite workpiece having adiabatic surface

The adiabatic top surface is an imaged surface. The coordinates of a point are related to the imaged coordinates by: (a) $\xi\eta = \xi'\eta'$; (b) $(\xi-\eta)/2+(\xi'-\eta')/2 = 2h'$, which indicate the same radius and the symmetry with respect to the adiabatic surface. Combining (a) and (b) gives

$$\xi' = 2h' - \tfrac{1}{2}(\xi-\eta) + \sqrt{[2h'-\tfrac{1}{2}(\xi-\eta)]^2+\xi\eta} \quad (8)$$

$$\eta' = -[2h'-\tfrac{1}{2}(\xi-\eta)] + \sqrt{[2h'-\tfrac{1}{2}(\xi-\eta)]^2+\xi\eta}. \quad (9)$$

Integrating ring-elements from 0 to ξ_e the temperature field yields

$$\theta = \frac{3Q^*\sqrt{S}}{\pi Pe}\left\{\exp\left(-\sqrt{\xi\eta}\cos\phi - \frac{\eta+\xi}{2}\right)\sum_{p=1}^{\infty}\right.$$

$$\times\left[\int_0^{\xi_e}\tilde{A}_{0,p}(\xi_i)\,d\xi_i\right]L^0_{p-1}(\xi)\Psi(p,1,\eta)$$

$$+\exp\left(-\sqrt{\xi'\eta'}\cos\phi - \frac{\eta'+\xi'}{2}\right)\sum_{p=1}^{\infty}$$

$$\left.\times\left[\int_0^{\xi_e}\tilde{A}_{0,p}(\xi_i)\,d\xi_i\right]L^0_{p-1}(\xi')\Psi(p,1,\eta')\right\} \quad \eta \geqslant \eta_0 \quad (10)$$

Without an image, the temperature is identical to eqn (18) in Ref. [15] for $\xi_e \to \infty$ [41]. That is, $A_{0,p}$ defined as eqn (19) in Ref. [15] equals the integration of $\tilde{A}_{0,p}$ over ξ_i from 0 to ∞. Assuming $\xi_e \to \infty$ and $\eta_0 \ll 1$ eqn (10) reduces to

$$\theta = \frac{3Q^*\sqrt{S\eta_0}}{\pi Pe}\exp(-\sqrt{\xi\eta}\cos\phi)$$

$$\times\left\{\sum_{p=1}^{\infty}\Gamma(p)\left(\frac{12\eta_0}{Pe^2}+\frac{1}{2}\right)^{-p}\left(\frac{12\eta_0}{Pe^2}-\frac{1}{2}\right)^{p-1}\right.$$

$$\times\left[\exp\left(-\frac{\eta+\xi}{2}\right)L^0_{p-1}(\xi)\Psi(p,1,\eta)\right.$$

$$\left.\left.+\exp\left(-\frac{\eta'+\xi'}{2}\right)L^0_{p-1}(\xi')\Psi(p,1,\eta')\right]\right\} \quad \eta \geqslant \eta_0 \quad (11)$$

where the coordinate of the cavity surface η_0 can be obtained from the momentum balance at the cavity base

$$\eta_0 = \frac{Pe[1+Y(\theta_B-1)]}{P\sqrt{S}}\exp\left[\frac{H(\theta_b-\theta_B)}{(\theta_B+\theta_\infty)(\theta_b+\theta_\infty)}\right]. \quad (12)$$

The coordinate of the cavity surface is related to the cavity depth by

$$h = \frac{r_0^2 Pe}{4\sqrt{S\eta_0}}. \quad (13)$$

The solution procedure is that: (i) an initial η_0 is guessed; (ii) the base temperature is calculated from eqn (11); (iii) an improve η_0 is obtained from eqn (12); (iv) steps (ii) and (iii) are repeated until η_0 converges; (v) the second law of thermodynamics is used to uniquely determine η_0; (vi) eqn (11) then describes the temperature field in the workpiece.

Since there are two cavities whose bases satisfy bal-

ances of momentum and energy [15], step (v) is required. Applying the second law of thermodynamics, the correct cavity is the one whose base temperature is increased with the dimensionless beam power.

Cooling rate and liquid temperature gradient-to-solidification speed ratio

In a quasi-steady-state cooling rates can be determined by [14]

$$\frac{\partial T}{\partial t} = -G_l U = -Pe\frac{\alpha(T_m - T_\infty)}{\hat{\sigma}^2}\frac{\partial \theta}{\partial x}. \quad (14)$$

On the other hand, the liquid temperature gradient-to-solidification speed ratio, $G_l/V_n = \nabla T_i \cdot \mathbf{n}/U\mathbf{i}\cdot\mathbf{n}$, where temperature $T_i \equiv T - T_m$ and the vector normal to the solidification front $\mathbf{n} = \nabla T_i/\|\nabla T_i\|$. The liquid temperature gradient-to-solidification speed ratio then becomes

$$\frac{G_l}{V_n} = \frac{(T_m - T_\infty)}{Pe\alpha}\frac{\|\nabla\theta\|^2}{\dfrac{\partial\theta}{\partial x}}. \quad (15)$$

Differentiating eqn (11) with respect to spatial coordinates to obtain the cooling rate and the liquid temperature gradient-to-solidification speed ratio is feasible but tedious. In this work, temperature gradients are conveniently discretized. Temperatures at grid points are then determined from eqn (11).

RESULTS AND DISCUSSION

In this study, independent parameters investigated are the dimensionless beam power (Q^*), Peclet number (Pe), cavity opening radius (r_0), preheating temperature (θ_∞), and parameter approximating convection (S). A good comparison between the predicted and measured dimensionless beam power per unit of penetration (Hicken *et al.* [20]) vs solid Peclet number for different liquid-to-solid diffusivity ratios is shown in Fig. 2. The effects of the liquid-to-solid diffusivity ratio on the beam power per unit of penetration become increasingly important as the solid Peclet number increases. In Fig. 3 the depthwise variation in a stability parameter predicted by this model show agreement with that obtained by Kou *et al.* [13]. An energy distribution parameter $\hat{\sigma} = 6.3 \times 10^{-4}$ m and a cavity opening radius $\hat{r}_0 = 4 \times 10^{-4}$ m were chosen to simulate a constant incident flux. The deviation of the solid–liquid interface predicted by Wei and Shian [15] and this work is shown in Fig. 4. Evidently, this study exhibits a perfect insulation at the top surface and smooth continuity at the cavity base. Using a more relevant image technique therefore is crucial.

The effects of Peclet number on the molten region around the cavity which is delineated by the circle on the top surface are shown in Fig. 5. An increase in Peclet number results in the molten region in the rear of the cavity to be more elongated while the molten

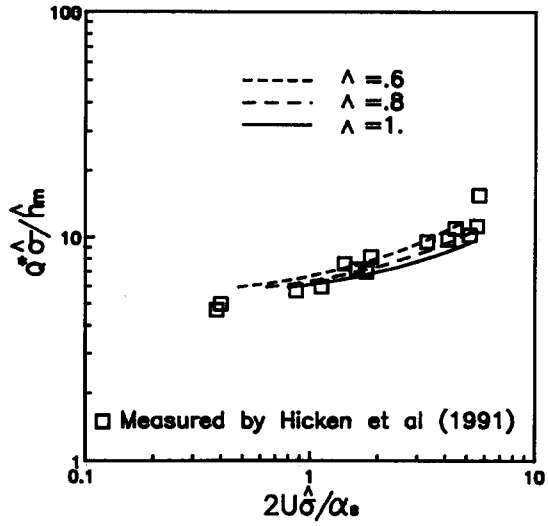

Fig. 2. Comparison of the predicted and measured power per unit of penetration vs solid Peclet number for different liquid-to-solid thermal diffusivity ratios in welding SS 304.

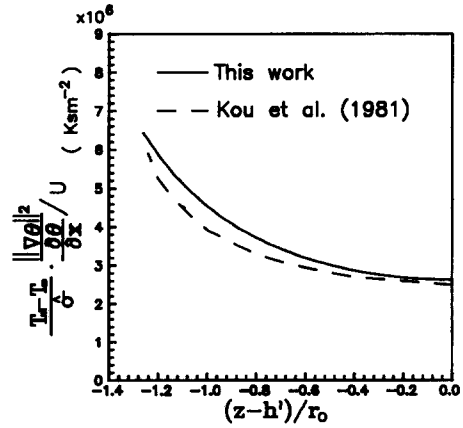

Fig. 3. Comparison of a stability parameter predicted by finite-difference result (Kou *et al.*, 1981) and this work.

layer on the side and near the front to be narrower. As presented in Figs. 6 and 7, depths of the cavity and fusion zone increase with reducing Peclet number and increasing the dimensionless beam power.

A quantitative evaluation of morphological stability was first derived by Tiller *et al.* [42] to be

$$\frac{G_l}{V_n} > -\frac{mC_0(1-k_e)}{k_e D} \quad (16)$$

which works well in most of solidification processing [43]. If the inequality in eqn (16) is satisfied the solidification front remains planar. Otherwise, the interface becomes unstable. The minimum liquid temperature gradient-to-solidification speed ratio at the trailing edge of the molten region therefore play an important role on the microstructure of the fusion zone.

Depthwise variations of the dimensionless cooling

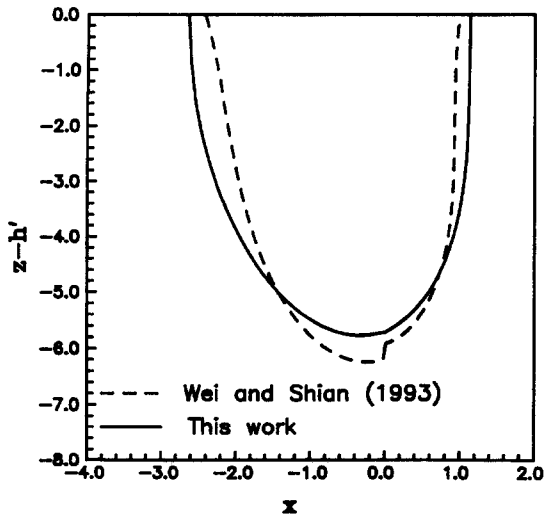

Fig. 4. Deviation of solid–liquid interface predicted by Wei and Shian (1993) and this work using different image methods.

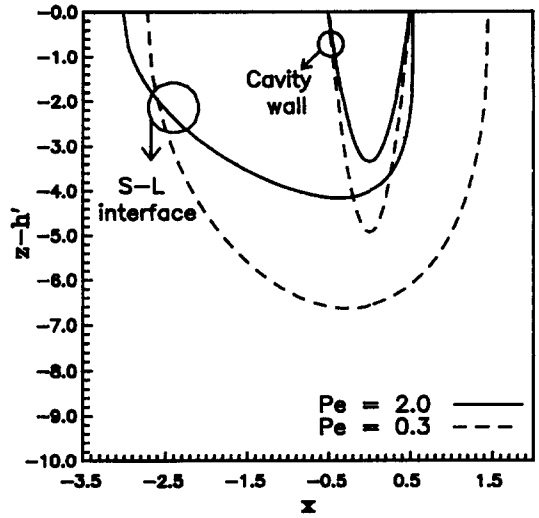

Fig. 6. Side view of molten regions for different Peclet numbers.

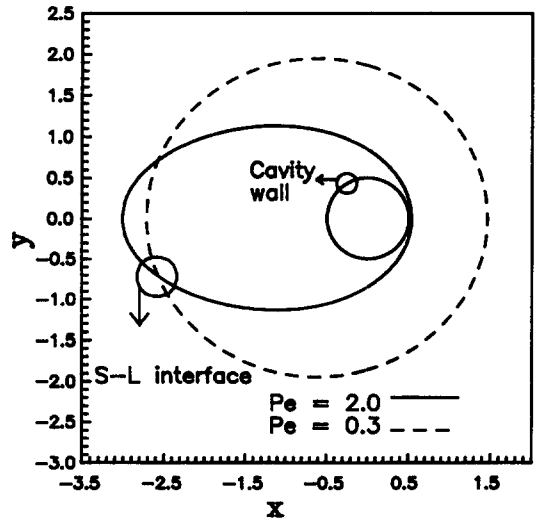

Fig. 5. Top view of molten regions for different Peclet numbers.

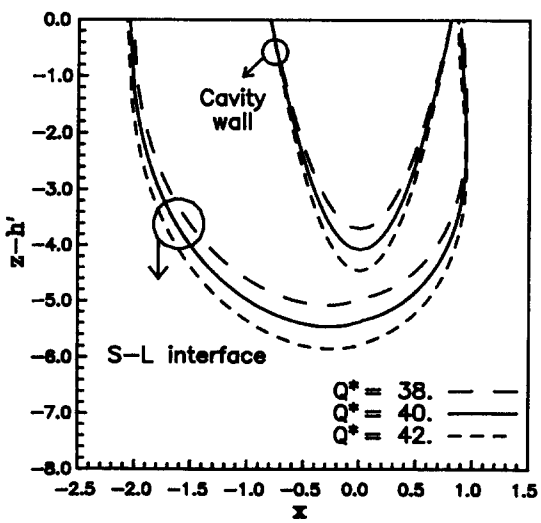

Fig. 7. Side view of molten regions for different dimensionless beam powers.

rate and liquid temperature gradient-to-solidification speed ratio on the solidification front at the trailing edge having an angle $\phi = \pi$ for different dimensionless beam powers are presented in Fig. 8. The left and right ordinates represent the dimensionless cooling rate and the dimensionless liquid temperature gradient-to-solidification speed ratio, respectively. The abscissa $z - h' = 0$ denotes the top surface of the workpiece. It is found that cooling rates increase slightly in the depthwise direction and drop rapidly to zero at the bottom of the molten region. The maximum dimensionless temperature gradient is around 0.4 which corresponds to 1260 K s^{-1} for welding aluminum with a welding speed of 10^{-2} m s^{-1} and energy distribution parameter of 0.002 m. This lies within a relevant range of cooling rates during electron- and laser-beam welding [44]. As the beam power decreases

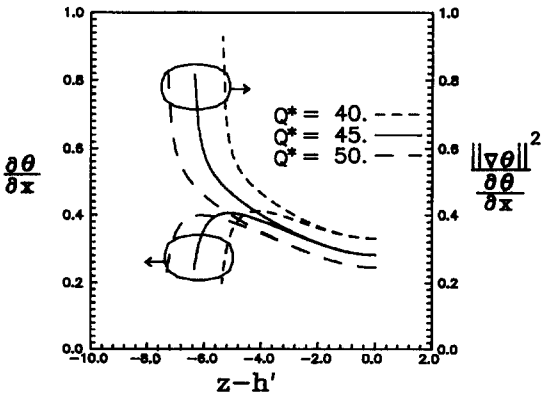

Fig. 8. Depthwise variation of dimensionless cooling rate and liquid temperature gradient-to-solidification speed ratio at angle $\phi = \pi$ for different dimensionless beam powers.

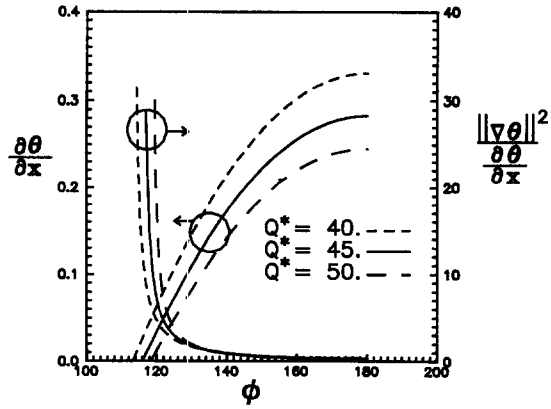

Fig. 9. Circumferential variation of dimensionless cooling rate and liquid temperature gradient-to-solidification speed ratio at top surface for different dimensionless beam powers.

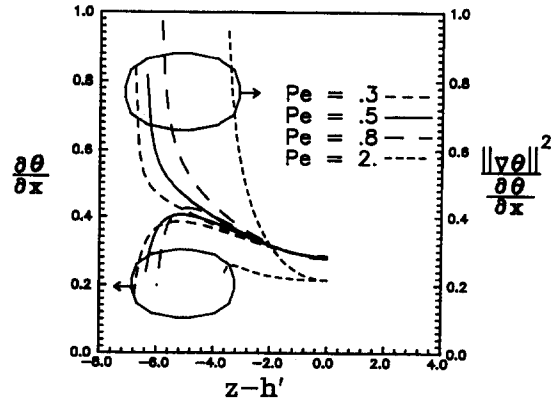

Fig. 10. Depthwise variation of dimensionless cooling rate and liquid temperature gradient-to-solidification speed ratio at angle $\phi = \pi$ for different Peclet numbers.

cooling rates increase near the top surface. This agrees with that obtained by the point- or line-source solution [45] and three-dimensional numerical computations [24].

The dimensionless liquid temperature gradient-to-solidification speed ratio exhibits a monotonic increase from the minimum at the top surface to infinity at the bottom of the molten region. Hence, the solidification front at the bottom is stable. In the case of dimensionless parameters $Q^* = 40$, $Pe = 0.5$ for the aluminum alloy containing 2 wt pct of Cu, a dimensionless liquid temperature gradient-to-solidification speed ratio near the bottom is 0.95 which corresponds to 3×10^7 K-sm^{-2}. Since the slope of the liquidus line in the phase diagram $m = -2.6$ K wt pct^{-1}, the equilibrium partition coefficient $k_e = 0.14$, and liquid thermal diffusivity $D = 3 \times 10^{-9}$ m^2 s^{-1}, respectively [46], the right-hand-side of eqn (16) yields 10^{10} K-sm^{-2}. Hence, the trailing edge is almost entirely unstable. As the dimensionless beam power increases morphological instability is enhanced. For a given dimensionless beam power the dimensionless cooling rate equals the dimensionless liquid temperature gradient-to-solidification speed ratio at the top surface. This is attributed to zero temperature gradients in depthwise and transverse directions.

Circumferential variations of the dimensionless cooling rate and liquid temperature gradient-to-solidification speed ratio at the top surface for different dimensionless beam powers are shown in Fig. 9. Evidently, cooling rates increase with the circumferential angle until the trailing edge is reached. A decrease in the dimensionless beam power increases cooling rates irrespective of the circumferential angle. The dimensionless liquid temperature gradient-to-solidification speed ratio decreases rapidly from infinity to $\partial\theta/\partial x$ corresponding to the locations at the maximum width of the molten region and the trailing edge, respectively. Hence, the most stale and unstable locations occur at the fusion boundary and weld centerline, respectively. This agrees with observations of planar and equiaxed substructures at the fusion boundary

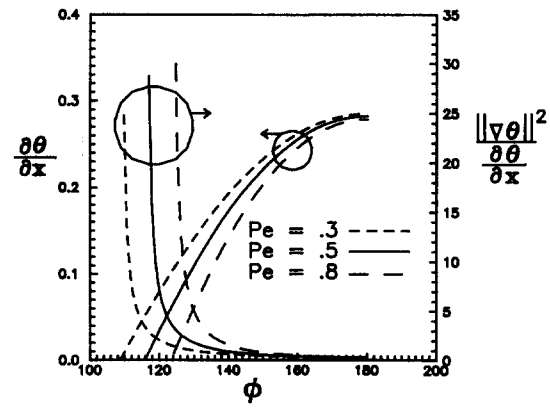

Fig. 11. Circumferential variation of dimensionless cooling rate and liquid temperature gradient-to-solidification speed ratio at top surface for different Peclet numbers.

and weld centerline, respectively. Morphological instability near the fusion boundary rather than the trailing edge is decreased by increasing the dimensionless beam power. The influence of the variation of the dimensionless beam power on morphological instability reduces as the circumferential angle increases.

As shown in the Figs. 10 and 11, a decrease of Peclet number increases dimensionless cooling rates near the top surface. The dimensional cooling rates, however, reduce with decreasing Peclet number. For example, dimensionless cooling rates at the trailing edge on the top surface are 0.29 and 0.22, which correspond to Peclet numbers of 0.3 and 2, respectively. Equation (14) then gives cooling rates of -1890 and -9560 K s^{-1}, respectively, for welding aluminum. On the other hand, as Peclet number decreases dimensionless liquid temperature gradient-to-solidification speed ratios increase near the top surface and trailing edge in contrast to the fusion boundary. The influence of the variations of Peclet number on morphological instability reduces near the trailing edge and top surface.

The effects of the dimensionless cavity opening radius on cooling rates and morphological instability

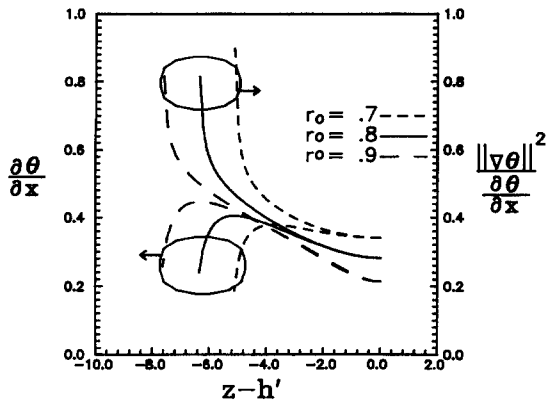

Fig. 12. Depthwise variation of dimensionless cooling rate and liquid temperature gradient-to-solidification speed ratio at angle $\phi = \pi$ for different dimensionless cavity opening radii.

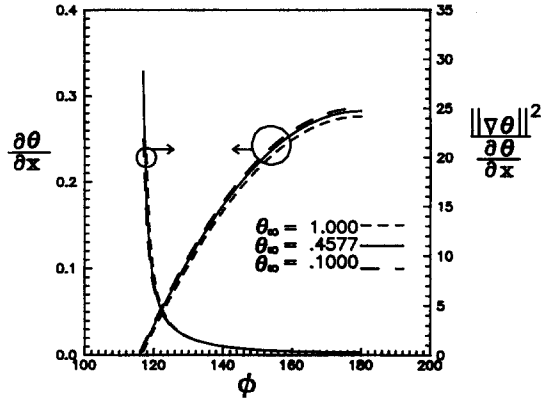

Fig. 14. Circumferential variation of dimensionless cooling rate and liquid temperature gradient-to-solidification speed ratio at top surface for different dimensionless preheating temperatures.

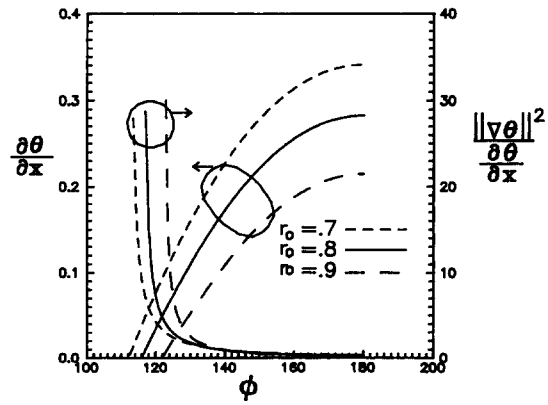

Fig. 13. Circumferential variation of dimensionless cooling rate and liquid temperature gradient-to-solidification speed ratio at top surface for different dimensionless cavity opening radii.

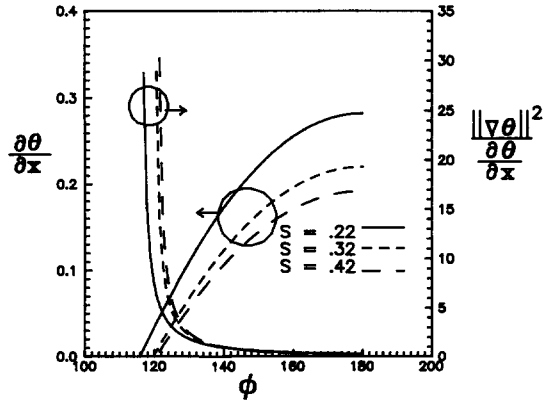

Fig. 15. Circumferential variation of dimensionless cooling rate and liquid temperature gradient-to-solidification speed ratio at top surface for different values of the parameter approximating convection.

are quite similar to that of the dimensionless beam power, as shown in Figs. 12 and 13. Evidently, increases in the dimensionless cavity opening radius and beam power imply a similar increase in energy absorbed by the cavity. As presented in Figs. 14 and 15, increases in the dimensionless preheating temperature and the parameter approximating convection reduce cooling rates near the top surface. Morphological instabilities near the trailing edge and top surface decrease with the dimensionless preheating temperature and parameter approximating convection. An enhanced morphological instability, however, occurs on the fusion boundary.

CONCLUSIONS

Conclusions drawn are the following:

(1) A three-dimensional temperature field governed by eqn (11) in the liquid and heat-affected zones around a welding cavity is provided. In view of the adiabatic top surface the heat conduction equation in the workpiece subject to a ring element of incident flux is solved first. Applying an image method to the solution and integrating over all rings analytical temperatures are then obtained.

(2) Three-dimensional fusion zone, cooling rates and morphological stability are predicted. The results agree with a measured relationship between the power per unit of penetration and solid Peclet number, and finite-difference computation of a stability parameter. An increase in cooling rates and decrease of the liquid temperature gradient-to-solidification speed ratio on the solidification front from the fusion boundary to weld centerline on a horizontal cross-section are also confirmed.

(3) An increase in Peclet number results in the length of the molten region in the rear of the cavity to increase and thicknesses of the molten layer in the front and on the side to decrease. Depths of the cavity and fusion zone are increased by reducing Peclet number and increasing the dimensionless beam power and cavity opening radius. The effects of other parameters on the shape of the fusion zone can also be readily obtained if they are required.

(4) The dimensionless cooling rates increase slightly in the depthwise direction and drop rapidly to

zero at the bottom of the molten region. Irrespective of the circumferential angle, the dimensional cooling rates near the top surface are enhanced by increasing Peclet number and decreasing the dimensionless beam power, cavity opening radius, preheating temperature, and the parameter approximating convection.

(5) The surface of the fusion zone has a stable or planar morphology because the liquid temperature gradient-to-solidification speed ratios are infinite. In other locations on the solidification front the liquid temperature gradient-to-solidification speed ratios drop to low values. Morphological instability near the trailing edge and top region of the molten pool rather than the fusion boundary increases with the dimensionless beam power, Peclet number, cavity opening radius, preheating temperature, and parameter approximating convection. The influence of the variations for these parameters on morphological instability reduces as the circumferential angle increases.

Acknowledgements—The authors acknowledge the financial support from the National Science Council, Taiwan, China, through Grant number NSC82-0401-E-110-061.

REFERENCES

1. Davies, G. J. and Garland, J. G., Solidification structures and properties of fusion welds. *International Metallurgical Reviews*, 1975, **20,** 83–106.
2. David, S. A., and Vitek, J. M., Correlation between solidification parameters and weld microstructures. *International Materials Review*, 1989, **34,** 213–245.
3. Calvo, F. A. C., Bentley, K. P. and Baker, R. G., Growth substructures in weld metal. *Acta Metallica*, 1960, **8,** 898–900.
4. Rutter, J. W. and Chalmers, B., A prismatic substructure formed during solidification of metals. *Canadian Journal of Physics*, 1953, **31,** 15–39.
5. Savage, W. F., Lundin, C. D. and Aronson, A. H., Weld metal solidification mechanics. *Welding Journal*, 1965, **44,** 175-s–181-s.
6. Matsuda, F., Hashimoto, T. and Senda, T., Fundamental investigations on solidification structure in weld metal. *Transactions of National Research Institute for Metals*, 1969, **11,** 43–58.
7. Kato, M., Matsuda, F. and Senda, T., Solidification mode in aluminum weld metal. *Transactions of the Japan Welding Society*, 1972, **3,** 69–76.
8. Brown, P. E. and Adams, Jr, C. M., Fusion-zone structures and properties in aluminum alloys. *Welding Journal*, 1960, **39,** 520-s–524-s.
9. Brown, P. E. and Adams, Jr, C. M., Rapidly solidified alloys structures. *Transactions of AFS*, 1961, **69,** 879–891.
10. Jordan, M. F. and Coleman, M. C., Fused zone structures in arc welded deposits of a commercial Al–Mg–Mn alloy. *British Welding Journal*, 1968, **15,** 553–558.
11. Lanzafame, J. N. and Kattamis, T. Z., Solidification structure and tensile properties of 2014 aluminum alloy welds. *Welding Journal*, 1973, **52,** 226-s–232-s.
12. Katayama, S. and Matsunawa, A., Solidification behaviour and microstructural characteristics of pulsed and continuous laser welded stainles steels. In *Laser Welding, Machining and Materials Processing. Proceedings of the International Conference on Applications of Lasers and Electro-optics ICALEO'85*, ed. C. Albright, 11–14 November, 1985, San Francisco, pp. 19–25.
13. Kou, S., Hsu, S. C. and Mehrabian, R., Rapid melting and solidification of a surface due to a moving heat flux. *Metallurgical Transactions*, 1981, **12B,** 33–45.
14. Rosenthal, D., Mathematical theory of heat distribution during welding and cutting. *Welding Journal*, 1941, **20,** 220-s–234-s.
15. Wei, P. S. and Shian, M. D., Three-dimensional analytical temperature field around the welding cavity produced by a moving distributed high-intensity beam. *ASME Journal of Heat Transfer*, 1993, **115,** 848–856.
16. Ol'shanskii, N. A., Movement of molten metal during electron-beam welding. *Svarochnoe Proizvodstvo*, 1974, **9,** 12–14.
17. Dowden, J., Davis, M. and Kapadia, P., Some aspects of the fluid dynamics of laser welding. *Journal of Fluid Mechanics*, 1983, **126,** 123–146.
18. Wei, P. S. and Giedt, W. H., Surface tension gradient-driven flow around an electron beam welding cavity. *Welding Journal*, 1985, **64,** 251-s–259-s.
19. Hsu, Y. F. and Rubinsky, B., Two-dimensional heat transfer study on the keyhole plasma arc welding process. *International Journal of Heat and Mass Transfer*, 1988, **31,** 1409–1421.
20. Hicken, G. K., Giedt, W. H. and Bentley, A. E., Correlation of joint penetration with electron beam current distribution. *Welding Journal*, 1991, **70,** 69-s–75-s.
21. Nippes, E. F. (coordinator). *Metals Handbook*, 9th edn, Vol. 6. ASM, Metals Park, OH, 1983.
22. Wang, S. C. and Wei, P. S., Energy-beam redistribution and absorption in a drilling or welding cavity. *Metallurgical Transactions*, 1992, **23B,** 505–511.
23. Ho, C. Y., Heat transfer in electron-beam welding. Ph.D. thesis, Institute of Mechanical Engineering, National Sun Yat-Sen University, Taiwan, China, 1996.
24. Wei, P. S., Wu, T. H. and Chow, Y. T., Investigation of high-intensity beam characteristics on welding cavity shape and temperature distribution. *ASME Journal of Heat Transfer*, 1990, **112,** 163–169.
25. Schauer, D. A., Giedt, W. H. and Shintaku, S. M., Electron beam welding cavity temperature distributions in pure metals and alloys. *Welding Journal*, 1978, **57,** 127-s–133-s.
26. Kristensen, J. K., Hansson, L. H. and Smidth, F. L., Key-hole formation, temperature distribution and thermal cycle in electron beam welding. In *Electron and Laser Beam Welding. Proceedings of the International Conference*, Tokyo, 14–15 July 1986, pp. 119–129.
27. Wei, P. S. and Chow, Y. T., Beam focusing characteristics and alloying element effects on high-intensity electron beam welding. *Metallurgical Transactions*, 1992, **23B,** 81–90.
28. Kaplan, A., A model of deep penetration laser welding based on calculation of the keyhole profile. *Journal of Physics D: Applied Physics*, 1994, **27,** 1805–1814.
29. Poueyo-Verwaerde, A., Fabbro, R., Deshors, G., de Frutos, A. M. and Orza, J. M., Experimental study of laser-induced plasma in welding conditions with continuous CO_2 laser. *Journal of Applied Physics*, 1993, **74,** 5773–5780.
30. Collur, M. M. and DebRoy, T., Emission spectroscopy of plasma during laser welding of AISI 201 stainless steel. *Metallurgical Transactions*, 1989, **20B,** 277–286.
31. Zel'dovich, Ya. B. and Raizer, Yu. P., *Physics of Shock Waves and High-Temperature Hydrodynamic Phenomena*, Chapter V, Vol. 1. Academic Press, New York, 1966.
32. Shui, V. H., Kivel, B. and Weyl, G. M., Effect of vapor plasma on the coupling of laser radiation with aluminum targets. *Journal of Quantitative Spectroscopy and Radiative Transfer*, 1978, **20,** 627–636.
33. Matsunawa, A. and Ohnawa, T., Beam-plume interaction in laser materials processing. *Transactions of Japan Welding Research Institute*, 1991, **20,** 9–15.
34. Dowden, J., Kapadia, P. and Postacioglu, N., An analy-

sis of the laser–plasma interaction in laser keyhole welding. *Journal of Physics D: Applied Physics*, 1989, **22,** 741–749.
35. Tix, C. and Simon, G., A transport theoretical model of the keyhole plasma in penetration laser welding. *Journal of Physics D: Applied Physics*, 1993, **26,** 2066–2074.
36. Duley, W. W., A comparison of keyhole absorption processes in laser and electron beam welding. In *Proceedings of the Conference on the Laser vs the Electron Beam in Welding, Cutting and Surface Treatment—State of the Art*—1987, ed. R. Bakish, Bakish Materials Corp., Englewood, N.J., 1987, pp. 160–167.
37. Wei, P. S. and Ho, J. Y., Energy considerations in high-energy beam drilling. *International Journal of Heat and Mass Transfer*, 1990, **33,** 2207–2217.
38. Wei, P. S. and Chiou, L. R., Molten metal flow around the base of a cavity during a high-energy beam penetrating process. *ASME Journal of Heat Transfer*, 1988, **110,** 918–923.
39. Gau, C. and Viskanta, R., Melting and solidification of a metal system in a rectangular cavity. *International Journal of Heat and Mass Transfer*, 1984, **27,** 113–123.
40. Giedt, W. H., Wei, X.-C. and Wei, S.-R., Effect of surface convection on stationary GTA weld zone temperatures. *Welding Journal*, 1984, **63,** 376-s–383-s.
41. Gradshteyn, I. S. and Ryzhik, I. M., *Table of Integrals, Series and Products*, ed. A. Jeffrey. Translated from the Russian by Scripta Technica, Inc., England, 1980, pp. 482 and 847.
42. Tiller, W. A., Jackson, K. A., Rutter, J. W. and Chalmers, B., The redistribution of solute atoms during the solidification of metals. *Acta Metallica*, 1953, **1,** 428–437.
43. Flemings, M. C., *Solidification Processing*, Chapter 3. McGraw-Hill, New York, 1974.
44. Elmer, J. W., Allen, S. M. and Eagar, T. W., Microstructural development during solidification of stainless steel alloys. *Metallurgical Translations*, 1989, **20A,** 2117–2131.
45. Adams, Jr, C. M., Cooling rates and peak temperatures in fusion welding. *Welding Journal*, 1958, **37,** 210-s–215-s.
46. Tewari, S. N. and Laxmanan, V., Cellular-dendritic transition in directionally solidified binary alloys. *Metallurgical Transactions*, 1987, **18A,** 167–170.